

Interacting-bath dynamical embedding for capturing non-local electron correlation in solids

Jiachen Li and Tianyu Zhu*

Department of Chemistry, Yale University, New Haven, CT 06520, USA

Abstract

Quantitative simulation of electronic structure of solids requires the treatment of local and non-local electron correlations on an equal footing. Dynamical mean-field theory, a widely-used quantum embedding algorithm that assumes local self-energy approximation, is challenging to extend to capture long-range electron correlation. In this work, we present a new formulation of Green's function embedding that, instead of embedding the impurity in non-interacting bath through the hybridization function, derives bath representation with general two-particle interactions in a fully *ab initio* and systematically improvable manner. The resulting interacting-bath dynamical embedding theory (ibDET) simulates local and non-local self-energies using high-level quantum chemistry solvers, such as the coupled-cluster theory. We demonstrate that ibDET combined with the *GW* theory (*GW*+ibDET) achieves good agreements with experimental band structure and photoemission spectra while preserving translational symmetry across a range of semiconducting, insulating, and metallic materials. Furthermore, our approach allows quantifying the role of non-local electron correlation in determining spectral properties of materials and addressing the long-standing debate over the bandwidth narrowing of metallic sodium.

arXiv:2406.07531v1 [cond-mat.mtrl-sci] 11 Jun 2024

* tianyu.zhu@yale.edu

INTRODUCTION

Predictive description of material-specific electronic properties in correlated electron systems remains a significant challenge in computational chemistry and physics [1]. The main reason is the need for quantitative treatment of electron correlation effects and simulating in the thermodynamic limit simultaneously. Quantum embedding theories offer a promising route to solve this problem [2], where a chosen active space of correlated states is embedded in an effective bath and then solved by high-level many-body theories, while the delocalized environment is described at the level of mean-field or low-order perturbation theories. For computing dynamical quantities, dynamical mean-field theory (DMFT) has been the most popular choice, leading to many advances in the understanding of correlated electron physics in lattice models and real materials [3–5].

Despite its success in treating strong local electron interactions, it is a long-standing challenge to extend DMFT to accurately capture long-range electron correlation in solids [6]. This capability is crucial for describing various quantum many-body phenomena, such as the pseudogap phase and stripe orders in high-temperature cuprate superconductors [7–9]. Cluster extensions in real (cluster DMFT, CDMFT [10–12]) or reciprocal (DCA and D Γ A [13–15]) spaces have been proposed previously, but these formalisms are mostly designed for short-range non-local correlation effects. Moreover, CDMFT is known to break translational invariance in periodic systems [16]. To account for band structure and long-range interactions in real materials, density functional theory (DFT) [17] or many-body perturbation theory (GW) [18–21] is normally adopted as the low-level theory for DMFT. Although much progress has been made in traditional DFT+DMFT [5] and GW +DMFT [22–25] formalisms within the downfolding scheme (Fig. 1a), they do not provide a truly quantitative *ab initio* treatment of local and non-local correlation effects due to several limitations. First, in downfolding-based DMFT, the impurity problem comprises a few strongly correlated orbitals representing a small low-energy subspace, but DFT/ GW +DMFT results could depend sensitively on the choice and construction of these impurity orbitals [26]. Second, the derivation of effective impurity interactions and approximation to their frequency dependence often introduce numerical uncertainties [27]. Third, an approximate double-counting correction scheme is needed to remove DFT contributions to the self-energy in DFT+DMFT calculations [28, 29]. Finally, the neglect of long-range interactions stronger than those captured by DFT or GW , are known to yield errors in a variety of settings [30], such as overestimation of 3s bandwidth and poor satellite prediction for metallic sodium by downfolded self-consistent GW +EDMFT [24].

To avoid downfolding-associated uncontrolled errors, one of us recently developed a full cell

GW +DMFT formalism [31, 32] (Fig. 1b), where the impurity problem comprises all local orbitals of atoms within a chosen unit cell or supercell. General bare Coulomb interactions within impurity orbitals are employed and solved by efficient high-level quantum chemistry solvers [33], removing the need for downfolding. The full cell embedding formalism in the context of DMFT and density matrix embedding theory (DMET) [34, 35] has shown promise in simulating challenging many-body problems at fully *ab initio* level beyond low-energy models, including the Kondo correlation in magnetic impurities [36] as well as the parent and superconducting states of cuprates [37, 38]. However, full cell GW +DMFT inevitably inherits certain limitations from cluster DMFT, such as the breaking of translational invariance. While the impurity space in full cell formalism is significantly increased, the non-local electron correlation beyond the selected supercell is at best captured at the GW level (we note, similar issue exists in the self-energy embedding theory [39, 40]). As a result, systematic convergence of non-local spectral properties towards the full system limit beyond GW has not been demonstrated.

A common origin of the non-local correlation challenge in DMFT is the *non-interacting* nature of its bath representation through the hybridization function. Although it is a natural choice for continuous-time quantum Monte Carlo (CTQMC) solvers [41], the non-interacting bath parametrization does not fully leverage the power of Hamiltonian-based solvers, such as exact diagonalization (ED) [42], density matrix renormalization group (DMRG) [43, 44], configuration interaction (CI) [45], and coupled-cluster (CC) theory [33, 46–48], as there is no clear mapping between the full Hamiltonian and the fictitious bath states. In this work, we build on our full cell embedding framework to develop a new Green’s function embedding formulation with *interacting* bath (Fig. 1c). We propose to project the full interacting Hamiltonian into multiple embedding spaces. Each embedding space consists of local orbitals of an impurity atom in the unit cell and systematically expanded bath orbitals, in which two-particle Coulomb interactions between all embedding orbitals are obtained through projection. This new formulation allows utilizing self-energy corrections to both impurity and bath states, computed by many-body solvers (CC in this work), for improving the description of dynamical quantities of the full system. Because we do not derive bath parameters by fitting the hybridization function, this method is, strictly speaking, no longer DMFT, and we term it interacting-bath dynamical embedding theory (ibDET). We demonstrate that GW +ibDET predicts accurate band structure and photoemission spectra across a range of semiconducting (silicon), insulating (2D BN, MgO, SrTiO₃), and metallic (sodium) materials against experiments and theoretical benchmarks. This work offers a new route towards precise treatment of local and non-local electron correlations in simulating material-specific spectral

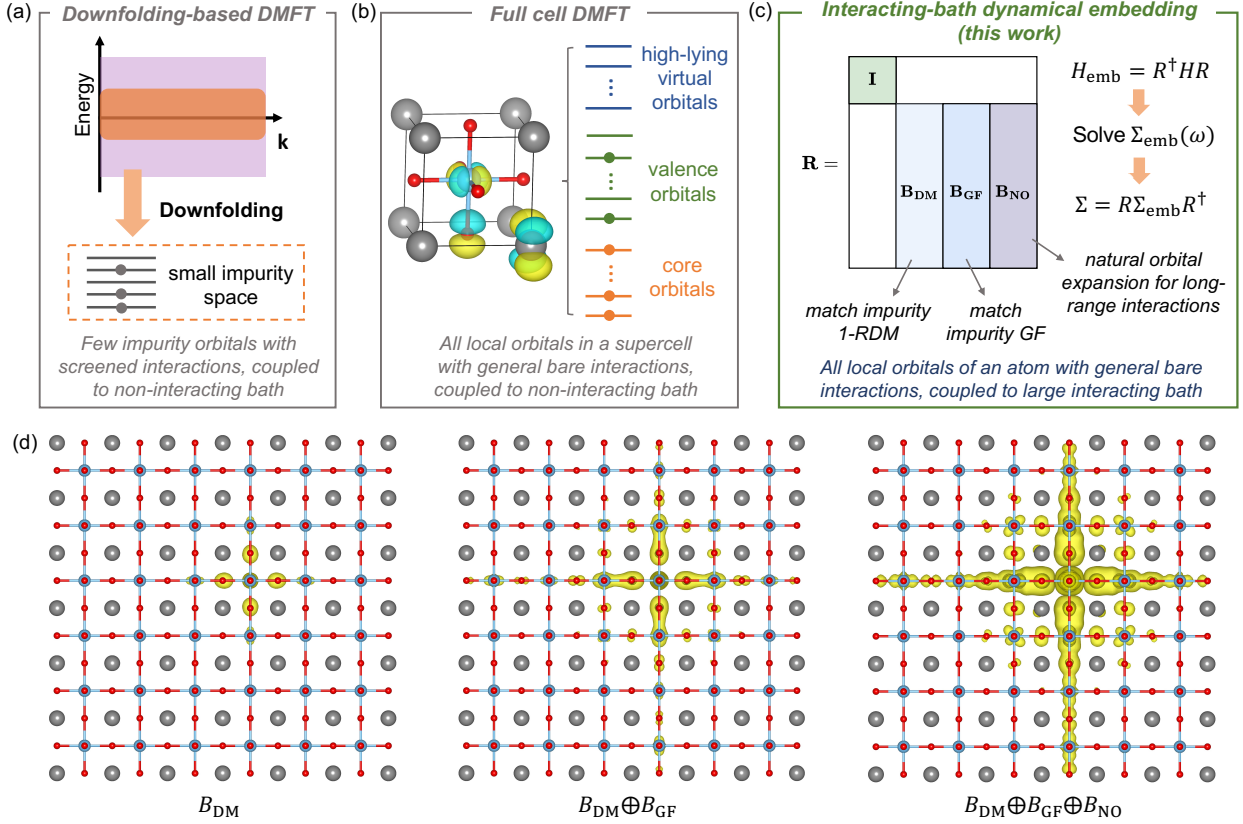


FIG. 1. Illustration of ibDET and previous DMFT formalisms. (a) Usual downfolding-based DFT/ GW +DMFT scheme. (b) Full cell GW +DMFT scheme. (c) Interacting-bath dynamical embedding scheme proposed in this work. In contrast, previous DMFT schemes all employ non-interacting bath representation. (b) Demonstration of real-space electron density in the embedding problem (impurity is a single Ti atom here) as the interacting bath is systematically expanded in SrTiO_3 .

properties of solids.

RESULTS

Interacting-bath dynamical embedding theory. Given a periodic crystal, we start with a mean-field solution at the Hartree-Fock (HF) or DFT level using crystalline Gaussian atomic orbitals. To define the impurity problem, we construct the orthogonal atom-centered local orbital basis employing an intrinsic atomic orbital plus projected atomic orbital (IAO+PAO) scheme [35, 49]. In this work, we choose all local orbitals on a single atom as the impurity and then gradually expand the bath space by selecting orbitals that entangle most strongly with impurity orbitals from the environment. To recover the self-energy of the full crystal, multiple embedding problems need to be formulated, each centered on an impurity atom in the unit cell (e.g., there are two embedding

problems for boron nitride: B-centered and N-centered).

The key step is then to perform algebraic construction of bath orbitals that allow direct projection from full Hamiltonian to the embedding space, a strategy that has proven successful in DMET simulations of ground-state properties [34, 35, 50]. The bath space in ibDET is designed for simulating excited-state properties, with three main components. The *first* set of bath orbitals B_{DM} is the same as in DMET, which is derived by a Schmidt decomposition, i.e., using the singular value decomposition (SVD) of the mean-field off-diagonal one-particle reduced density matrix (1-RDM) between the impurity and remaining lattice [35]. The role of B_{DM} is to ensure that impurity 1-RDM is exactly reproduced in the embedding calculation at the mean-field level. The *second* set of bath orbitals B_{GF} is obtained by performing SVD of the imaginary part of mean-field off-diagonal Green’s function $g(\omega_n)$ on a uniform real-frequency grid, to capture the frequency-dependent entanglement between impurity and environment [51], a role similar to that of the hybridization function in DMFT. To keep the number of B_{DM} and B_{GF} orbitals tractable, we couple bath orbitals only to valence impurity orbitals (i.e., IAOs) and adopt an additional projection to orthogonalize the embedding space, which also removes a large number of redundant B_{GF} orbitals that have minimal overlap with the lattice Hilbert space. As shown in Fig. 1d, B_{DM} and B_{GF} only span a local real space around the impurity, suggesting they do not capture non-local electron correlation beyond short range. Thus, we employ a *third* set of cluster-specific natural bath orbitals B_{NO} inspired by local correlation methods in quantum chemistry [52], which was introduced to quantum embedding by Nusspickel and Booth recently [50]. The idea is to select natural orbitals from the environment that correlate strongly to the existing embedding cluster ($I \oplus B_{\text{DM}} \oplus B_{\text{GF}}$, where I stands for the impurity space), enabled by a relatively cheap direct second-order perturbation theory (MP2) calculation (see Methods for details). B_{NO} can be systematically expanded by incorporating environmental orbitals with largest orbital entropy, which is crucial for accounting for long-range electron correlation (see Fig. 1d). In practice, we also include a few extra low-lying conduction bands into the bath space, since they improve the description of band gaps in semiconductors and insulators (see SI for details).

The Hamiltonian for each embedding problem is then written as

$$H_{\text{emb}} = \sum_{ij}^{\text{emb}} \tilde{F}_{ij} a_i^\dagger a_j + \frac{1}{2} \sum_{ijkl}^{\text{emb}} (ij|kl) a_i^\dagger a_k^\dagger a_l a_j \quad (1)$$

where $(ij|kl)$ is the general two-particle bare Coulomb interaction matrix defined on all impurity and bath orbitals, obtained through a projection with rotation matrix R (see Fig. 1c for the

definition of R). The one-particle interaction matrix is defined as

$$\tilde{F}_{ij} = F_{ij}^{\text{emb}} - \sum_{kl}^{\text{emb}} \gamma_{kl}^{\text{emb}} [(ij|lk) - \frac{1}{2}(ik|lj)]. \quad (2)$$

Here, F^{emb} is obtained through rotation $F^{\text{emb}} = R^\dagger F^{\text{full}} R$, where F^{full} is the Fock matrix of the full system computed using HF (even when we start from the DFT density), and γ^{emb} is the mean-field density matrix rotated to the embedding space. The HF contribution to the self-energy is exactly removed from the one-particle interaction matrix, so there is no double counting in ibDET.

Coupled-cluster Green's function (CCGF) solver at the EOM-CCSD level [33] is adopted to solve the embedding Hamiltonians (Eq. 1) directly on the real axis. We choose the CCGF solver because of its good performance for various lattice models and real materials [53–57], as well as high computational efficiency (can treat more than 200 orbitals). In the meantime, we emphasize that ibDET can in principle utilize any Hamiltonian-based solvers, such as quantum chemistry DMRG [44] and selected configuration interaction [58]. The self-energy computed within the embedding space is then rotated back to the full Hilbert space

$$\Sigma^{\text{full},J}(\omega) = R \Sigma^{\text{emb},J}(\omega) R^\dagger, \quad (3)$$

where J means the J -th embedding problem. The self-energy matrices $\{\Sigma^{\text{full},J}(\omega)\}$ from all embedding calculations are then assembled using a democratic partitioning scheme and Fourier transformed to the momentum space, to obtain the full self-energy of the crystal $\Sigma^{\text{ibDET}}(\mathbf{k}, \omega)$. Similar to GW +DMFT, ibDET can be combined with the GW theory to capture any small long-range correlation effects missed by ibDET, and the resulting GW +ibDET self-energy is

$$\Sigma^{GW+\text{ibDET}}(\mathbf{k}, \omega) = \Sigma^{GW,\text{full}}(\mathbf{k}, \omega) + \Sigma^{\text{CC},\text{ibDET}}(\mathbf{k}, \omega) - \Sigma^{GW,\text{ibDET}}(\mathbf{k}, \omega), \quad (4)$$

where $\Sigma^{GW,\text{full}}$ is the GW self-energy of the full system. Different from common DFT+DMFT and GW +DMFT calculations that require self-consistency, we only discuss the application of one-shot ibDET in this work.

Convergence of ibDET results towards full system limit. We first demonstrate numerical convergence of ibDET results on silicon (Si) and two-dimensional hexagonal boron nitride (2D BN), where full EOM-CCSD benchmarks are available. For Si, GTH-cc-pVTZ basis set [59] and GTH-HF-rev pseudopotential [60] were employed, together with $4 \times 4 \times 4$ \mathbf{k} -point sampling. For 2D BN, GTH-DZVP basis set [61] and GTH-PADE pseudopotential as well as $6 \times 6 \times 1$ \mathbf{k} -mesh were adopted. In the case of Si, even for a medium $4 \times 4 \times 4$ \mathbf{k} -mesh, it is not feasible to run full CCSD and EOM-CCSD calculations, thus we used a composite correction scheme introduced in Ref. [62]

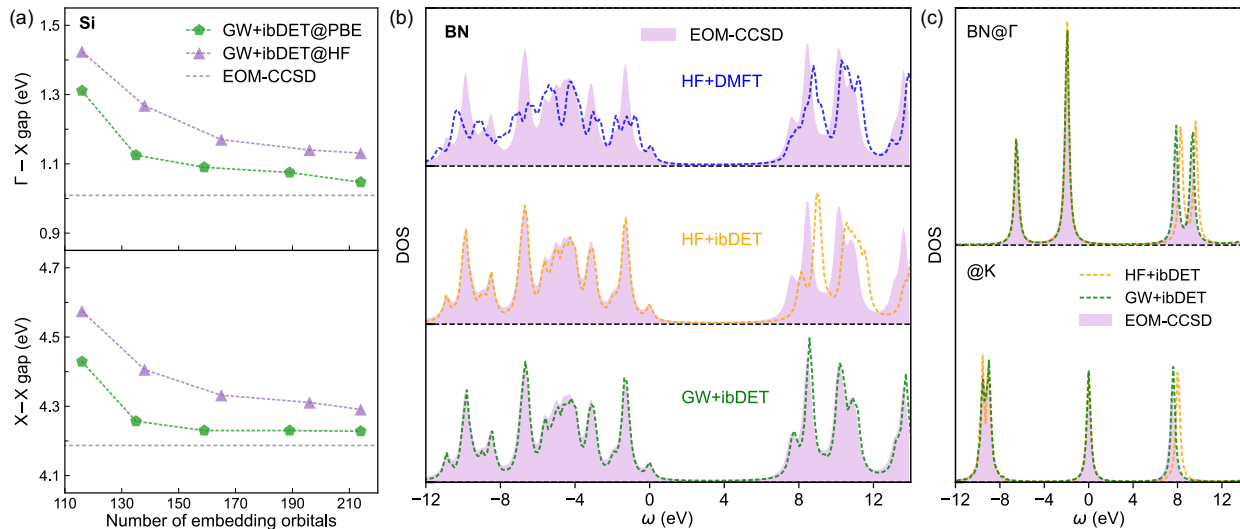


FIG. 2. Benchmark of ibDET results against full EOM-CCSD on silicon and 2D BN. (a) Convergence of $GW+ibDET$ direct and indirect band gaps in silicon ($4 \times 4 \times 4$ \mathbf{k} -mesh) as the number of embedding orbitals is increased. G_0W_0 starting from HF or PBE reference state was used as the low-level theory. (b) DOS of 2D BN ($6 \times 6 \times 1$ \mathbf{k} -mesh) obtained from HF+ibDET and $GW+ibDET$ ($G_0W_0@HF$ was used as the low-level theory), compared against full cell HF+DMFT [32] and EOM-CCSD. A broadening factor of 0.2 eV is used. (c) Momentum-resolved DOS of 2D BN at Γ and K points.

to estimate EOM-CCSD band gaps. All calculations were conducted based on the PySCF quantum chemistry software package [63, 64].

In Fig. 2a, we show the convergence of $GW+ibDET$ predictions of silicon band gaps against the full system limit (i.e., EOM-CCSD). We choose this small band-gap system because of the long-range nature of its screened Coulomb interaction, which is particularly challenging for quantum embedding methods that assume a local self-energy approximation (e.g., DMFT). Although one-shot G_0W_0 approximation on top of GGA (generalized gradient approximation) functionals is known to predict accurate band structure for Si, this success benefits from error cancellations, indicated by the large difference between $G_0W_0@PBE$ (1.15 eV) and $G_0W_0@HF$ (1.86 eV) Γ -X band gaps. As shown in Fig. 2a, the $GW+ibDET$ predicted band gaps quickly converge to the full EOM-CCSD limit as the embedding space grows. At around 210 embedding orbitals (less than 6% of the number of orbitals in full system), the $GW+ibDET$ (PBE reference) Γ -X and X-X band gap errors against EOM-CCSD are both only 0.04 eV. Furthermore, since the long-range electron correlation is mostly captured by CCGF solver within ibDET, the starting point dependence is significantly reduced in $GW+ibDET$ from 0.71 eV to 0.08 eV (Γ -X gap) when using PBE vs. HF reference.

Next, we show *ibDET* also predicts accurate photoemission spectrum, using 2D BN as an example (Fig. 2b). Previous full cell HF+DMFT simulation with a BN unit cell as the impurity yields accurate band gaps, but the calculated spectrum shape shows some discrepancies (especially the valence part) [32], an indication of broken translational symmetry. In contrast, the density of states (DOS) predicted by HF+*ibDET* (200 orbitals in each embedding space) is in good agreement with full EOM-CCSD, suggesting the treatment of non-local electron correlation is substantially improved. The valence spectrum is near perfect, although the band gap is overestimated due to the large error in HF. *GW*+*ibDET* (HF reference), on the other hand, further improves over HF+*ibDET* and achieves quantitative agreement with EOM-CCSD over a wide frequency range (the band gap error is smaller than 0.1 eV). Inspection of the momentum-resolved DOS (Fig. 2c) demonstrates that the band degeneracy in HF+*ibDET* and *GW*+*ibDET* spectra agrees well with that in EOM-CCSD, because the translational symmetry is well preserved in *ibDET*.

MgO and SrTiO₃. We then apply *GW*+*ibDET* to study two metal oxides (MgO and SrTiO₃) and compare against available experimental measurements. MgO is a weakly correlated insulator with experimental band gap of 7.98~8.19 eV [62, 65] (zero-point renormalization corrected), but it is a challenging system for the *GW* theory. G_0W_0 @PBE underestimates the band gap (7.43 eV[20]) while quasiparticle self-consistent *GW* (QS*GW*) largely overestimates (9.33 eV[21]). We performed *GW*+*ibDET* (PBE reference) calculation of MgO using all-electron cc-pVTZ basis set and $6 \times 6 \times 6$ **k**-point sampling, with 230 orbitals in each embedding space. As presented in Table I and Fig. 3a, *GW*+*ibDET* greatly improves over G_0W_0 @PBE and predicts the band gap to be 8.22 eV, in better agreement with experimental values. We note that our *GW*+*ibDET* value is also consistent with recent EOM-CCSD benchmark on MgO (8.34 eV[62]), and the slight difference is likely due to different basis sets and treatments of finite size errors.

We next show results for a moderately correlated perovskite-type insulator strontium titanate (SrTiO₃), with experimental indirect band gap of 3.25 eV. Although SrTiO₃ has no open-shell 3*d* electrons, its lowest conduction bands are dominated by localized Ti-3*d* orbitals, causing severe underestimation of the band gap by LDA (local density approximation) and GGA functionals (e.g., 1.82 eV by PBE as seen in Table I). On the other hand, G_0W_0 @PBE overestimates the band gap (3.62 eV), while various self-consistent *GW* schemes are known to yield even larger overestimation errors [66, 67]. We conducted *GW*+*ibDET* calculations using all-electron def2-TZVP basis set [68] for Ti, def2-SVP basis set for O, and GTH-DZVP-MOLOPT-SR/GTH-HF-rev basis/pseudopotential for Sr, with $6 \times 6 \times 6$ **k**-mesh. As seen in Table I and Fig. 3b, with around 210 embedding orbitals in each embedding space, *GW*+*ibDET* (PBE reference) predicts the R- Γ

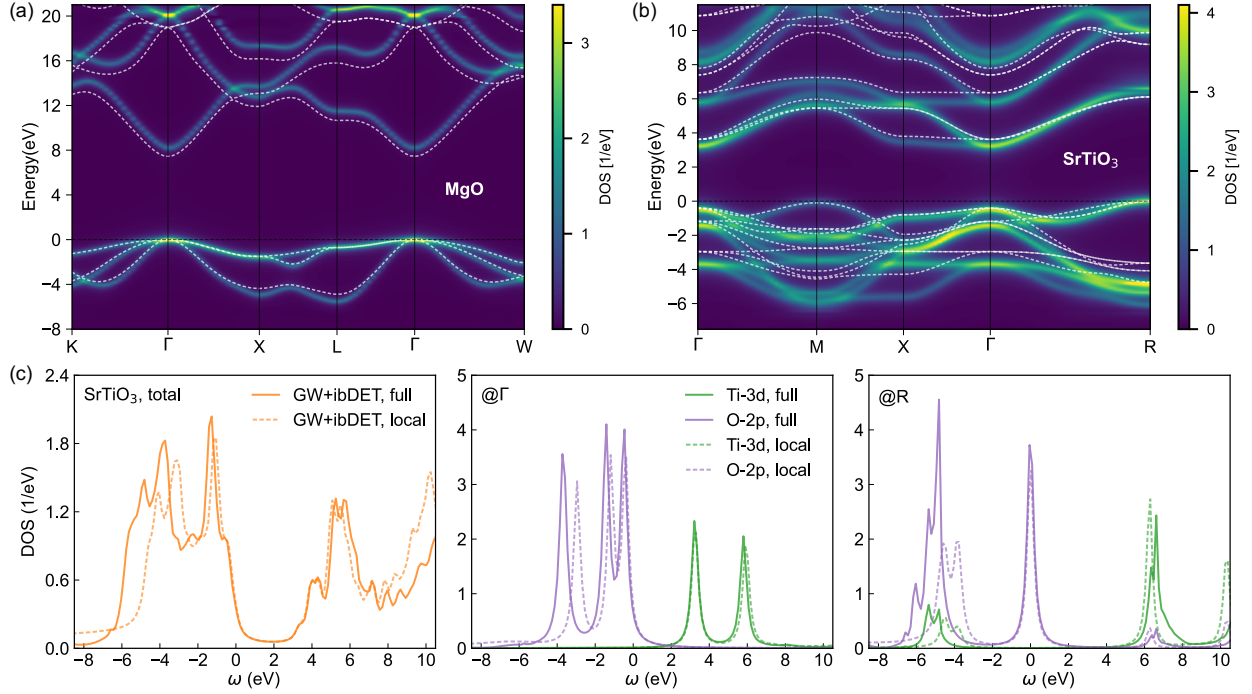


FIG. 3. (a) Band structure of MgO computed by $GW+ibDET$ (heat map). $G_0W_0@PBE$ is shown for comparison (white dashes). A broadening factor of 0.2 eV is used. (b) Band structure of SrTiO₃ computed by $GW+ibDET$ (heat map). $G_0W_0@PBE$ is shown for comparison (white dashes). A broadening factor of 0.2 eV is used. (c) Effects of non-3d-orbital vertex corrections to the self-energy ($\Sigma^{CC} - \Sigma^{GW}$) on the total and momentum-resolved $GW+ibDET$ DOS in SrTiO₃. The self-energy corrections are added to all orbitals (“full”) or only Ti-3d orbitals (“local”).

and Γ - Γ band gaps to be 3.24 eV and 3.74 eV, in excellent agreement with experimental values, indicating that $ibDET$ provides a balanced description of local and non-local electron correlations beyond GW . Comparing the $G_0W_0@PBE$ and $GW+ibDET$ band structures, we also find that $GW+ibDET$ predicts broader valence band spectrum due to the shift of O-dominant peaks by 1~2 eV.

To understand how non-local correlation affects the predicted spectral function of SrTiO₃, we further compare DOS obtained from the normal $GW+ibDET$ calculation versus DOS calculated with only local self-energy correction ($\Sigma^{CC} - \Sigma^{GW}$) to Ti-3d orbitals (Fig. 3c). We find that, the total DOS around the Fermi level is not affected much because the main contribution to the lowest conduction bands comes from local Ti-3d orbitals. However, the positions of O-2p valence peaks change substantially when the non-3d-orbital vertex corrections to the self-energy are included. Moreover, even Ti-3d peaks are shifted in momentum-resolved DOS due to hybridization with other orbitals, as seen in Fig. 3c (R point), which suggests that non-local electron correlation

captured by ibDET is crucial for achieving a quantitative description of the band structure of SrTiO₃.

TABLE I. Summary of GW +ibDET (PBE reference) results for MgO, SrTiO₃ and Na, compared against PBE, G_0W_0 @PBE, and experimental values. All values are in eV.

	MgO		SrTiO ₃		Na
	Γ - Γ	X- Γ	Γ - Γ	R- Γ	Bandwidth
Experiment	7.98[65], 8.19[62]		3.75[69]	3.25[69]	2.65[70], 2.78[71]
PBE	4.74	5.92	2.22	1.82	3.41
G_0W_0 @PBE	7.45	8.94	4.03	3.62	3.20
GW +ibDET	8.22	9.74	3.74	3.24	2.84

Metallic sodium. We finally apply ibDET to study metallic sodium (Na), which is traditionally considered as a near-free-electron weakly correlated metal. DFT with LDA or GGA functional severely overestimates the occupied 3s bandwidth of Na (PBE bandwidth calculated in this work is 3.41 eV) compared to those measured by angle-resolved photoemission spectroscopy (ARPES) experiments (2.65~2.78 eV) [70, 71], which leads to long-standing debate over the nature of electron correlation in Na [24, 72–76]. Adding non-local static exchange in hybrid functionals yields even worse results [73], indicating that many-body dynamical correlation effects are needed to explain the bandwidth narrowing. The GW approximation is also insufficient, as one-shot G_0W_0 method only slightly improves over LDA and GGA, for example, our calculated G_0W_0 @PBE bandwidth is 3.20 eV (3.15 eV from G_0W_0 @LDA [73]). Single-site DFT+DMFT and self-consistent GW +EDMFT have also been applied to this problem, where the impurity is a single Na-3s orbital. A good agreement was obtained by LDA+eDMFT (2.84 eV) in Ref. [73], which resulted in the conclusion that only local electron correlation within single Na atom needs to be captured beyond DFT for predicting accurate bandwidth. However, Ref. [24] showed contradictory result (3.2~3.3 eV, no improvement over GW) from GW +EDMFT, which suggested treating Na-Na non-local correlation beyond GW is important for simulating metallic sodium. Such discrepancy is likely due to the use of different effective interactions within the downfolding scheme.

We thus apply ibDET, which is free of downfolding and treats significantly larger embedding space (225 orbitals), to address this puzzle. We note that, the CCGF solver was previously shown to agree very well with numerically exact DMRG on the spectral function of a small uniform electron gas model at the relevant Wigner-Seitz radius $r_s = 4$ [72]. Our GW +ibDET (PBE reference) simulation employed GTH-cc-pVTZ basis set [59] and GTH-HF-rev pseudopotential, as well as

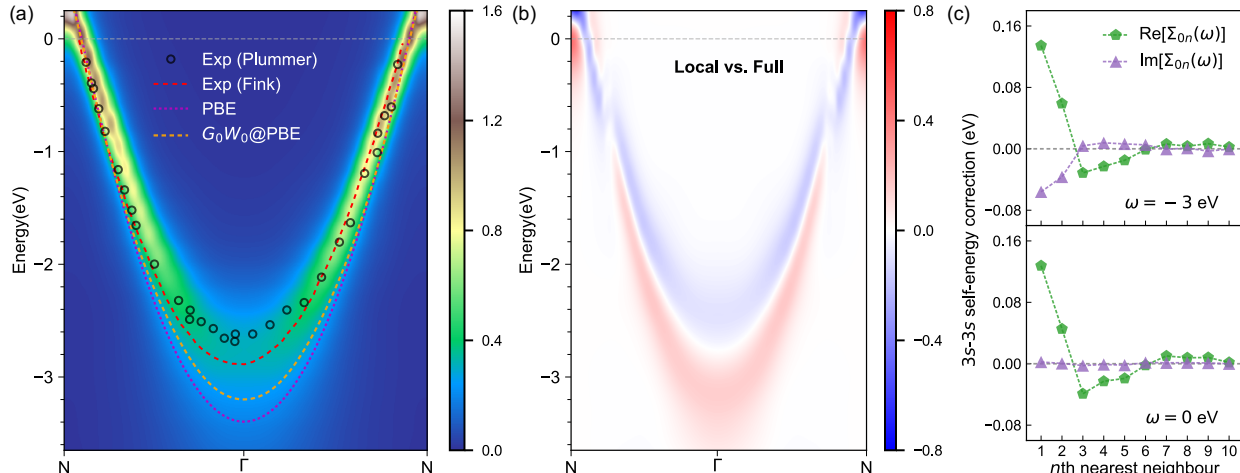


FIG. 4. $GW+ibDET$ results for metallic sodium. A broadening factor of 0.2 eV is used. (a) Band structure computed by $GW+ibDET$ (heat map), compared against PBE, $G_0W_0@PBE$, and ARPES experiments by Plummer et al. [70] and Fink et al. [71]. (b) Difference between two photoemission spectra, DOS(“Local”) – DOS(“Full”), computed by applying self-energy correction ($\Sigma^{CC} - \Sigma^{GW}$) to the full system (“Full”) or only to the diagonal block within each Na atom (“Local”). (c) Decay of inter-atomic 3s-3s non-local self-energy correction ($\Sigma^{CC} - \Sigma^{GW}$) between Na atoms at two frequencies, as the Na-Na distance increases.

$8 \times 8 \times 8$ \mathbf{k} -point sampling, which corresponds to 4608 electrons (512 valence electrons) in 12800 spatial orbitals. As shown in Fig. 4a, we find that $GW+ibDET$ achieves excellent agreement with the ARPES spectra [70, 71] and predicts an occupied bandwidth of 2.84 eV (note: the experimental bandwidth of 2.78 eV is from a more recent ARPES experiment with higher resolution [71]), significantly better than $G_0W_0@PBE$ and PBE.

Now that we have established the accuracy of $GW+ibDET$, we further analyze the nature of electron correlation in metallic sodium. Specifically, we ask if the same good bandwidth prediction can be obtained with only local self-energy approximation, by limiting the $\Sigma^{CC} - \Sigma^{GW}$ self-energy correction to the diagonal block of the full self-energy matrix within each Na atom (this approximation is similar to single-site DFT+DMFT and $GW+EDMFT$). In Fig. 4b, we find that, without non-local inter-atomic self-energy correction beyond GW , the bandwidth predicted by “local” $GW+ibDET$ is 3.11 eV, only slightly improved over $G_0W_0@PBE$ (3.20 eV) and much worse than that predicted by full $GW+ibDET$ (2.84 eV), which reveals the importance of non-local correlation effects. Furthermore, $GW+ibDET$ allows us to quantify the magnitude of real-space long-range electron correlation within the sodium supercell. In Fig. 4c, we plot how inter-atomic 3s-3s self-energy correction ($\Sigma^{CC} - \Sigma^{GW}$) changes as the Na-Na atom distance increases, at $\omega = 0$ eV (Fermi level) and $\omega = -3$ eV (around the bandwidth energy level). We find that the real part of

$3s$ - $3s$ self-energy correction does not decay to zero until 6th nearest neighbour in distance, indicating the electron correlation is indeed quite delocalized in metallic sodium. Thus, to quantitatively simulate spectral properties of sodium, we argue it is crucial to account for long-range electron correlation at a many-body level beyond DFT and GW , as seen in $GW+ibDET$.

DISCUSSION

We have developed a new Green’s function embedding formulation, interacting-bath dynamical embedding theory, for capturing local and non-local electron correlations on an equal footing in quantum many-body simulation of solids. In contrast to conventional DMFT approaches that derive downfolded impurity problems coupled to non-interacting bath, we systematically expand the bath space surrounding all local orbitals of impurity atoms without the need for downfolding or hybridization function fitting, which allows the construction of embedding Hamiltonian with general bare Coulomb interaction through simple projection. The main strength of this method is that it avoids uncontrolled errors associated with small impurity subspace and empirical truncations, while fully leveraging the power of advanced quantum chemistry solvers for treating long-range electron correlation effects. We have demonstrated that the $GW+ibDET$ approach achieves quantitative description of spectral properties across a wide range of materials, while preserving the translational invariance, which conventional cluster DMFT methods fail to do. In particular, $ibDET$ provides a unique capability to examine the effect of non-local (and even long-range) electron correlation in determining material-specific electronic properties of correlated electron systems, as illustrated in the case of metallic sodium. $GW+ibDET$ is thus a promising tool for tackling material problems in which non-local electron correlation plays a significant role. Moving forward, we hope that the $ibDET$ approach proposed in this work stimulates further development of DMFT extensions and other quantum embedding methods beyond local correlation approximation, towards a predictive many-body toolbox for simulating correlated electron materials.

METHODS

Construction of bath orbitals. In $ibDET$, mean-field (HF and DFT) and GW calculations of the full crystal are performed in the \mathbf{k} -space. The embedding problem is formulated on a local orbital (LO) basis in the real space, where the intrinsic atomic orbital plus projected atomic orbital (IAO+PAO) [35, 49] scheme is used. In this work, all local orbitals on each atom within

the unit cell are chosen as the impurity, and the bath space is expanded by selecting orbitals that entangle most strongly with impurity orbitals from the environment. Because calculations are performed in both \mathbf{k} -space and real space, the Fourier transform is utilized to convert quantities such as density matrix, Green’s function, and self-energy between the two spaces when needed. The details of the Fourier transform can be found in the SI. A main task in ibDET is to perform algebraic construction of bath orbitals that allow direct mapping between the full Hilbert space and the embedding space. Three components are employed to construct the bath orbitals in a systematically improvable manner.

Firstly, bath orbitals B_{DM} that were originally developed in DMET [35, 77] are computed. For a chosen impurity, B_{DM} are obtained from the Schmidt decomposition, i.e., the SVD of the mean-field off-diagonal 1-RDM between the impurity and remaining lattice

$$\gamma^{\text{imp,env}} = B_{\text{DM}}\Lambda V^\dagger \quad (5)$$

where γ is the supercell mean-field 1-RDM in the LO basis. The resulting bath orbitals B_{DM} ensure that the impurity 1-RDM is exactly reproduced in the embedding calculation at the mean-field level. Also, a property of Schmidt decomposition is that the number of bath orbitals is no more than the number of impurity orbitals. Furthermore, we choose to only couple B_{DM} (and later B_{GF}) to the valence impurity orbitals (i.e., IAOs) to reduce the number of bath orbitals, because we mainly focus on the low-energy physics around the Fermi level.

Secondly, to capture the dynamical (frequency-dependent) entanglement between the impurity and its environment, we derive bath orbitals B_{GF} to ensure that the one-particle Green’s function of the impurity is accurately reproduced in the embedding calculation at the mean-field level. Motivated by the fact that the Green’s function at the static time limit is the 1-RDM $\gamma = \lim_{\tau \rightarrow 0^-} G(\tau)$, we discretize the mean-field Green’s function $g(\omega_n)$ on a uniform set of real-axis frequency points $\{\omega_n\}$ as the “dynamical” extension to the “static” B_{DM} [51]. Here, the role of B_{GF} is similar to that of the hybridization function fitting in DMFT. We first calculate the occupied and virtual parts of the \mathbf{k} -space mean-field Green’s function $g_{\text{occ}}^{\text{MO}}(\mathbf{k}, \omega)$ and $g_{\text{vir}}^{\text{MO}}(\mathbf{k}, \omega)$

$$(g_{\text{occ}}^{\text{MO}})_{mn}(\mathbf{k}, \omega) = \delta_{mn} \frac{f_{\mathbf{k}m}}{\omega - \epsilon_{\mathbf{k}m} + i\eta} \quad (6)$$

$$(g_{\text{vir}}^{\text{MO}})_{mn}(\mathbf{k}, \omega) = \delta_{mn} \frac{(1 - f_{\mathbf{k}m})}{\omega - \epsilon_{\mathbf{k}m} + i\eta} \quad (7)$$

where m, n are the molecular orbitals (bands), $f_{\mathbf{k}m}$ is the Fermi-Dirac occupation number, $\epsilon_{\mathbf{k}m}$ is the mean-field molecular orbital energy, and η is a small broadening factor. $g_{\text{occ}}^{\text{MO}}(\mathbf{k}, \omega)$ and

$g_{\text{vir}}^{\text{MO}}(\mathbf{k}, \omega)$ are then rotated to the LO basis

$$g_{\text{occ}}^{\text{LO}}(\mathbf{k}, \omega) = C^{\mathbf{k}, \text{MO}, \text{LO}\dagger} g_{\text{occ}}^{\text{MO}}(\mathbf{k}, \omega) C^{\mathbf{k}, \text{MO}, \text{LO}} \quad (8)$$

$$g_{\text{vir}}^{\text{LO}}(\mathbf{k}, \omega) = C^{\mathbf{k}, \text{MO}, \text{LO}\dagger} g_{\text{vir}}^{\text{MO}}(\mathbf{k}, \omega) C^{\mathbf{k}, \text{MO}, \text{LO}} \quad (9)$$

where $C^{\mathbf{k}, \text{MO}, \text{LO}}$ is the transformation matrix from the molecular orbital (MO) basis to the LO basis. After Fourier transforming $g_{\text{occ}}^{\text{LO}}(\mathbf{k}, \omega)$ and $g_{\text{vir}}^{\text{LO}}(\mathbf{k}, \omega)$ to the supercell representation in real space $g_{\text{occ}}(\mathbf{R}, \omega)$ and $g_{\text{vir}}(\mathbf{R}, \omega)$, the occupied and the virtual bath orbitals $B_{\text{GF}, \text{occ}}$ and $B_{\text{GF}, \text{vir}}$ are obtained with the SVD of the imaginary part of the mean-field off-diagonal Green's functions ($g_{\text{occ}}(\mathbf{R}, \omega)$ and $g_{\text{vir}}(\mathbf{R}, \omega)$) between the impurity and remaining lattice

$$\text{Im}g_{\text{occ}}^{\text{imp, env}}(\omega_n) = [B_{\text{GF}, \text{occ}} \Lambda V^\dagger] (\omega_n) \quad (10)$$

$$\text{Im}g_{\text{vir}}^{\text{imp, env}}(\omega_n) = [B_{\text{GF}, \text{vir}} \Lambda V^\dagger] (\omega_n) \quad (11)$$

The bath orbitals B_{GF} are then assembled as

$$B_{\text{GF}} = [B_{\text{GF}, \text{occ}}(\omega_1), B_{\text{GF}, \text{vir}}(\omega_1), B_{\text{GF}, \text{occ}}(\omega_2), B_{\text{GF}, \text{vir}}(\omega_2), \dots] \quad (12)$$

We note that, this bath discretization results in a large number of B_{GF} orbitals, while many of them are redundant. To keep the number of embedding orbitals tractable, we apply a projection step detailed in a subsection below, to remove the embedding orbitals that overlap minimally with the original Hilbert space and orthogonalize the embedding space. As shown in Fig. 1d, the embedding space $I \oplus B_{\text{DM}} \oplus B_{\text{GF}}$ (I is impurity space) spans a local real space around the impurity, which covers the short- and medium-range electron correlations.

To capture long-range electron correlation within ibDET, we also incorporate the cluster-specific natural orbitals [50] to expand the existing embedding space $I \oplus B_{\text{DM}} \oplus B_{\text{GF}}$. As demonstrated in Ref. 50, the correlated density matrices are constructed in two subspaces to select bath orbitals with strongest couplings to the embedding space. The first subspace comprises occupied orbitals from the embedding space and virtual orbitals from the environment, permitting only excitations from the embedding space to the environment. By diagonalizing the virtual-virtual block of the correlated density matrix in this subspace, the virtual natural orbitals with dominant correlations (indicated by the magnitude of orbital entropy, i.e., the extent of fractional occupancy) to the embedding space are selected. Concurrently, the second subspace includes occupied orbitals from the environment and virtual orbitals from the embedding space, which leads to the occupied natural

orbitals with dominant correlations to the embedding space. This can be illustrated as

$$\text{emb-occ} + \text{env-vir} \rightarrow \gamma^{\text{vir,vir}} \rightarrow B_{\text{NO,vir}} \quad (13)$$

$$\text{env-occ} + \text{emb-vir} \rightarrow \gamma^{\text{occ,occ}} \rightarrow B_{\text{NO,occ}} \quad (14)$$

In this work, we use the direct MP2 [78] approach to construct the correlated density matrix, which is computationally less demanding and provides similar results compared to full MP2 [79]. The virtual-virtual and occupied-occupied blocks of the direct MP2 density matrix are

$$\gamma_{\tilde{a}\tilde{b}} = \sum_i^{\text{emb,occ}} \sum_{\tilde{c}}^{\text{env,vir}} t_{ii}^{\tilde{a}\tilde{c}} t_{ii}^{\tilde{c}\tilde{b}} \quad (15)$$

$$\gamma_{\tilde{i}\tilde{j}} = 2\delta_{\tilde{i}\tilde{j}} - \sum_{\tilde{k}}^{\text{env,occ}} \sum_a^{\text{emb,vir}} t_{i\tilde{k}}^{aa} t_{\tilde{k}j}^{aa} \quad (16)$$

where the direct MP2 amplitudes are $t_{ii}^{\tilde{a}\tilde{b}} = \frac{(i\tilde{a}|\tilde{i}\tilde{b})}{\epsilon_{\tilde{a}} + \epsilon_{\tilde{b}} - 2\epsilon_i}$ and $t_{i\tilde{j}}^{aa} = \frac{(i\tilde{a}|\tilde{j}a)}{2\epsilon_a - \epsilon_i - \epsilon_{\tilde{j}}}$. Here, we use i, j, k for indexes of occupied orbitals, a, b, c for indexes of virtual orbitals, while the tilde sign above the index means the orbital is in the environment. The computational scaling of direct MP2 in Eqs. 15 and 16 is $\mathcal{O}(O_{\text{emb}}V_{\text{env}}^3)$ and $\mathcal{O}(O_{\text{env}}^3V_{\text{emb}})$, where O_{emb} and V_{emb} are the numbers of occupied and virtual orbitals in the embedding space, and O_{env} and V_{env} are the numbers of occupied and virtual orbitals in the environment. We find that, for each embedding problem, typically 100~200 B_{NO} bath orbitals (corresponding to a direct MP2 fractional occupancy threshold of $10^{-3} \sim 10^{-5}$) are sufficient to converge $GW+ib\text{DET}$ spectral properties close to the full system limit.

In addition to natural bath orbitals obtained from direct MP2, a few (typically 15) low-lying canonical orbitals (conduction bands) are incorporated into the embedding space, which improves the description of band gaps in insulators and semiconductors. This is motivated by previous works showing that natural orbitals derived from configuration interaction singles (CIS) or CIS with perturbative doubles [CIS(D)] [80, 81] are often needed for describing excited states in local correlation based methods. As shown in the SI, we find that adding canonical orbitals performs similarly well as adding CIS or CIS(D) natural orbitals, while keeping the computational cost low.

Combining three components of bath orbitals, the embedding space can be expressed as $I \oplus B_{\text{DM}} \oplus B_{\text{GF}} \oplus B_{\text{NO}}$. As shown in Fig. 1d, long-distance components are included to the final embedding space, which are important for describing the long-range electron correlation.

Reduction of the embedding space. Adding different components of bath orbitals introduced above can result in a large number of embedding orbitals. However, many of these bath orbitals are not orthogonal to each other and may have a small overlap with the full Hilbert space.

Therefore, the size of the expanded embedding space can be significantly reduced by projecting out redundant bath orbitals. We define a projection operator

$$\hat{P} = |\text{imp}\rangle \langle \text{imp}| + |\text{bath}\rangle \langle \text{bath}| \quad (17)$$

Then the occupied and virtual orbitals of full Hilbert space are projected onto two subspaces defined by \hat{P} , which leads to two overlap matrices

$$\hat{P}_{ij}^{\text{occ}} = \langle \psi_i | \hat{P} | \psi_j \rangle \quad (18)$$

$$\hat{P}_{ab}^{\text{vir}} = \langle \psi_a | \hat{P} | \psi_b \rangle \quad (19)$$

By separately diagonalizing the overlap matrices within two distinct subspaces (the magnitude of eigenvalue λ indicates the extent of overlap), the embedding orbitals are orthonormalized. Moreover, we only keep the embedding orbitals with substantial overlap with the full Hilbert space, controlled by an eigenvalue threshold $\lambda > 0.01$.

Self-energy assembly. In ibDET, the impurity is defined as all local orbitals on each atom within the unit cell. For a system with N_{atom} atoms in the unit cell, N_{atom} embedding problems are solved (the embedding problem centered around the I -th impurity atom is denoted as the I -th embedding calculation). To restore the full-space self-energy Σ^{full} , for the I -th embedding problem, we rotate the self-energy calculated by impurity solvers from the embedding space $\Sigma^{\text{emb},I}(\omega)$ to the full space $\Sigma^{\text{full},I}(\omega)$ according to Eq. 3. We then use N_{atom} $\{\Sigma^{\text{full},I}\}$ to assemble the final ibDET self-energy Σ^{full} following a democratic partitioning scheme. The diagonal block within each atom $\Sigma_{II}^{\text{full}}$ is taken to be the self-energy $\Sigma_{II}^{\text{full},I}$ obtained from the I -th embedding calculation, while the off-diagonal block between the I -th atom and the J -th atom is taken as the average between $\Sigma_{IJ}^{\text{full},I}$ and $\Sigma_{IJ}^{\text{full},J}$ from two separate embedding calculations. For example, for a system with a two-atom unit cell, the full-space self-energy is assembled as

$$\Sigma^{\text{full}} = \begin{bmatrix} \Sigma_{11}^{\text{full},1} & \frac{1}{2} \left(\Sigma_{12}^{\text{full},1} + \Sigma_{12}^{\text{full},2} \right) \\ \frac{1}{2} \left(\Sigma_{21}^{\text{full},2} + \Sigma_{21}^{\text{full},1} \right) & \Sigma_{22}^{\text{full},2} \end{bmatrix} \quad (20)$$

With the assembled self-energy from Eq. 20, the ibDET Green's function is evaluated through the Dyson's equation

$$G(\omega) = \left[g^{-1}(\omega) - \Sigma^{\text{full}}(\omega) \right]^{-1}. \quad (21)$$

ACKNOWLEDGMENTS

This work was supported by the National Science Foundation under Grant No. CHE-2337991 and a start-up fund from Yale University. J.L. also acknowledges support from the Tony Massini Postdoctoral Fellowship in Data Science from Yale University.

DATA AVAILABILITY

Data used in this work are available in the main text and supplementary information.

CODE AVAILABILITY

The ibDET code will be open-sourced upon publication of this manuscript. The ibDET implementation uses the fcDMFT package, which is available at <https://github.com/ZhuGroup-Yale/fcdmft>, as well as PySCF, which is available at <https://github.com/pyscf/pyscf>.

AUTHOR CONTRIBUTIONS

J.L. and T.Z. designed the project, developed the ibDET algorithm and code, and wrote the manuscript. J.L. performed ibDET numerical simulations. T.Z. supervised the project.

ADDITIONAL INFORMATION

Supplementary information is available for this paper.

-
- [1] P. R. Kent and G. Kotliar, Toward a Predictive Theory of Correlated Materials, *Science* **361**, 348 (2018).
 - [2] Q. Sun and G. K.-L. Chan, Quantum Embedding Theories, *Acc. Chem. Res.* **49**, 2705 (2016).
 - [3] A. Georges and G. Kotliar, Hubbard Model in Infinite Dimensions, *Phys. Rev. B* **45**, 6479 (1992).
 - [4] A. Georges, G. Kotliar, W. Krauth, and M. J. Rozenberg, Dynamical Mean-Field Theory of Strongly Correlated Fermion Systems and the Limit of Infinite Dimensions, *Rev. Mod. Phys.* **68**, 13 (1996).
 - [5] G. Kotliar, S. Y. Savrasov, K. Haule, V. S. Oudovenko, O. Parcollet, and C. A. Marianetti, Electronic Structure Calculations with Dynamical Mean-Field Theory, *Rev. Mod. Phys.* **78**, 865 (2006).

- [6] G. Rohringer, H. Hafermann, A. Toschi, A. A. Katanin, A. E. Antipov, M. I. Katsnelson, A. I. Lichtenstein, A. N. Rubtsov, and K. Held, Diagrammatic routes to nonlocal correlations beyond dynamical mean field theory, *Rev. Mod. Phys.* **90**, 025003 (2018).
- [7] M. Hashimoto, I. M. Vishik, R.-H. He, T. P. Devereaux, and Z.-X. Shen, Energy Gaps in High-Transition-Temperature Cuprate Superconductors, *Nat. Phys.* **10**, 483 (2014).
- [8] B. X. Zheng, C. M. Chung, P. Corboz, G. Ehlers, M. P. Qin, R. M. Noack, H. Shi, S. R. White, S. Zhang, and G. K. L. Chan, Stripe order in the underdoped region of the two-dimensional Hubbard model, *Science* (80-.). **358**, 1155 (2017).
- [9] H. Xu, C. M. Chung, M. Qin, U. Schollwöck, S. R. White, and S. Zhang, Coexistence of superconductivity with partially filled stripes in the Hubbard model, *Science* (80-.). **384**, eadh7691 (2024).
- [10] A. I. Lichtenstein and M. I. Katsnelson, Antiferromagnetism and d-wave superconductivity in cuprates: A cluster dynamical mean-field theory, *Phys. Rev. B* **62**, R9283 (2000).
- [11] G. Kotliar, S. Y. Savrasov, G. Pálsson, and G. Biroli, Cellular Dynamical Mean Field Approach to Strongly Correlated Systems, *Phys. Rev. Lett.* **87**, 186401 (2001).
- [12] G. Biroli and G. Kotliar, Cluster Methods for Strongly Correlated Electron Systems, *Phys. Rev. B* **65**, 155112 (2002).
- [13] M. Hettler, A. Tahvildar-Zadeh, M. Jarrell, and T. Pruschke, Nonlocal dynamical correlations of strongly interacting electron systems, *Phys. Rev. B* **58**, R7475 (1998).
- [14] T. Maier, M. Jarrell, T. Pruschke, and M. H. Hettler, Quantum Cluster Theories, *Rev. Mod. Phys.* **77**, 1027 (2005).
- [15] A. Toschi, A. A. Katanin, and K. Held, Dynamical vertex approximation: A step beyond dynamical mean-field theory, *Phys. Rev. B* **75**, 045118 (2007).
- [16] M. Klett, N. Wentzell, T. Schäfer, F. Simkovic, O. Parcollet, S. Andergassen, and P. Hansmann, Real-space cluster dynamical mean-field theory: Center-focused extrapolation on the one- and two particle-levels, *Phys. Rev. Res.* **2**, 033476 (2020).
- [17] W. Kohn and L. J. Sham, Self-Consistent Equations Including Exchange and Correlation Effects, *Phys. Rev.* **140**, A1133 (1965).
- [18] M. S. Hybertsen and S. G. Louie, Electron Correlation in Semiconductors and Insulators: Band Gaps and Quasiparticle Energies, *Phys. Rev. B* **34**, 5390 (1986).
- [19] D. Golze, M. Dvorak, and P. Rinke, The GW compendium: A practical guide to theoretical photoemission spectroscopy, *Front. Chem.* **7**, 377 (2019).
- [20] T. Zhu and G. K.-L. Chan, All-Electron Gaussian-Based G_0W_0 for Valence and Core Excitation Energies of Periodic Systems, *J. Chem. Theory Comput.* **17**, 727 (2021).
- [21] J. Lei and T. Zhu, Gaussian-Based Quasiparticle Self-Consistent GW for Periodic Systems, *J. Chem. Phys.* **157**, 214114 (2022).
- [22] P. Sun and G. Kotliar, Extended Dynamical Mean-Field Theory and \mathbf{GW} Method, *Phys. Rev. B* **66**, 085120 (2002).

- [23] S. Biermann, F. Aryasetiawan, and A. Georges, First-Principles Approach to the Electronic Structure of Strongly Correlated Systems: Combining the *GW* Approximation and Dynamical Mean-Field Theory, *Phys. Rev. Lett.* **90**, 086402 (2003).
- [24] F. Nilsson, L. Boehnke, P. Werner, and F. Aryasetiawan, Multitier Self-Consistent *GW*+EDMFT, *Phys. Rev. Mater.* **1**, 043803 (2017).
- [25] J. Tomczak, P. Liu, A. Toschi, G. Kresse, and K. Held, Merging *GW* with DMFT and Non-Local Correlations Beyond, *Eur. Phys. J. Spec. Top.* **226**, 2565 (2017).
- [26] J. Karp, A. Hampel, and A. J. Millis, Dependence of DFT+DMFT results on the construction of the correlated orbitals, *Phys. Rev. B* **103**, 195101 (2021).
- [27] F. Aryasetiawan, M. Imada, A. Georges, G. Kotliar, S. Biermann, and A. I. Lichtenstein, Frequency-Dependent Local Interactions and Low-Energy Effective Models from Electronic Structure Calculations, *Phys. Rev. B* **70**, 195104 (2004).
- [28] X. Wang, M. J. Han, L. de' Medici, H. Park, C. A. Marianetti, and A. J. Millis, Covalency, double-counting, and the metal-insulator phase diagram in transition metal oxides, *Phys. Rev. B* **86**, 195136 (2012).
- [29] L. Muechler, D. I. Badrtdinov, A. Hampel, J. Cano, M. Rösner, and C. E. Dreyer, Quantum embedding methods for correlated excited states of point defects: Case studies and challenges, *Phys. Rev. B* **105**, 235104 (2022).
- [30] A. L. Kutepov, Spatial non-locality of electronic correlations beyond *GW* approximation, *J. Phys. Condens. Matter* **33**, 485601 (2021).
- [31] T. Zhu and G. K.-L. Chan, Ab Initio Full Cell *GW*+DMFT for Correlated Materials, *Phys. Rev. X* **11**, 021006 (2021).
- [32] T. Zhu, Z.-H. Cui, and G. K.-L. Chan, Efficient Formulation of Ab Initio Quantum Embedding in Periodic Systems: Dynamical Mean-Field Theory, *J. Chem. Theory Comput.* **16**, 141 (2020).
- [33] T. Zhu, C. A. Jiménez-Hoyos, J. McClain, T. C. Berkelbach, and G. K.-L. Chan, Coupled-Cluster Impurity Solvers for Dynamical Mean-Field Theory, *Phys. Rev. B* **100**, 115154 (2019).
- [34] G. Knizia and G. K.-L. Chan, Density Matrix Embedding: A Simple Alternative to Dynamical Mean-Field Theory, *Phys. Rev. Lett.* **109**, 186404 (2012).
- [35] Z.-H. Cui, T. Zhu, and G. K.-L. Chan, Efficient Implementation of Ab Initio Quantum Embedding in Periodic Systems: Density Matrix Embedding Theory, *J. Chem. Theory Comput.* **16**, 119 (2020).
- [36] T. Zhu, L. Peng, H. Zhai, Z.-H. Cui, and G. K.-L. Chan, Towards an exact electronic quantum many-body treatment of kondo correlation in magnetic impurities, *arXiv preprint arXiv:2405.18709* (2024).
- [37] Z.-H. Cui, H. Zhai, X. Zhang, and G. K.-L. Chan, Systematic electronic structure in the cuprate parent state from quantum many-body simulations, *Science* **377**, 1192 (2022).
- [38] Z.-H. Cui, J. Yang, J. Tölle, H.-Z. Ye, H. Zhai, R. Kim, X. Zhang, L. Lin, T. C. Berkelbach, and G. K.-L. Chan, Ab initio quantum many-body description of superconducting trends in the cuprates, *arXiv preprint arXiv:2306.16561* (2023).

- [39] A. A. Rusakov, S. Iskakov, L. N. Tran, and D. Zgid, Self-energy embedding theory (SEET) for periodic systems, *J. Chem. Theory Comput.* **15**, 229 (2019).
- [40] S. Iskakov, C.-N. Yeh, E. Gull, and D. Zgid, *Ab Initio* Self-Energy Embedding for the Photoemission Spectra of NiO and MnO, *Phys. Rev. B* **102**, 085105 (2020).
- [41] E. Gull, A. J. Millis, A. I. Lichtenstein, A. N. Rubtsov, M. Troyer, and P. Werner, Continuous-time Monte Carlo methods for quantum impurity models, *Rev. Mod. Phys.* **83**, 349 (2011).
- [42] A. Liebsch and H. Ishida, Temperature and bath size in exact diagonalization dynamical mean field theory, *J. Phys. Condens. Matter* **24**, 053201 (2012).
- [43] E. Ronca, Z. Li, C. A. Jimenez-Hoyos, and G. K.-L. Chan, Time-Step Targeting Time-Dependent and Dynamical Density Matrix Renormalization Group Algorithms with *Ab Initio* Hamiltonians, *J. Chem. Theory Comput.* **13**, 5560 (2017).
- [44] H. Zhai, H. R. Larsson, S. Lee, Z. H. Cui, T. Zhu, C. Sun, L. Peng, R. Peng, K. Liao, J. Tölle, J. Yang, S. Li, and G. K. L. Chan, Block2: A comprehensive open source framework to develop and apply state-of-the-art DMRG algorithms in electronic structure and beyond, *J. Chem. Phys.* **159**, 234801 (2023).
- [45] D. Zgid, E. Gull, and G. K.-L. Chan, Truncated configuration interaction expansions as solvers for correlated quantum impurity models and dynamical mean-field theory, *Phys. Rev. B* **86**, 165128 (2012).
- [46] M. Nooijen and J. G. Snijders, Coupled cluster Green’s function method: Working equations and applications, *Int. J. Quantum Chem.* **48**, 15 (1993).
- [47] B. Peng and K. Kowalski, Green’s Function Coupled-Cluster Approach: Simulating Photoelectron Spectra for Realistic Molecular Systems, *J. Chem. Theory Comput.* **14**, 4335 (2018).
- [48] A. Shee and D. Zgid, Coupled Cluster as an Impurity Solver for Green’s Function Embedding Methods, *J. Chem. Theory Comput.* **15**, 6010 (2019).
- [49] G. Knizia, Intrinsic Atomic Orbitals: An Unbiased Bridge between Quantum Theory and Chemical Concepts, *J. Chem. Theory Comput.* **9**, 4834 (2013).
- [50] M. Nusspickel and G. H. Booth, Systematic Improvability in Quantum Embedding for Real Materials, *Phys. Rev. X* **12**, 011046 (2022).
- [51] M. Nusspickel and G. H. Booth, Efficient Compression of the Environment of an Open Quantum System, *Phys. Rev. B* **102**, 165107 (2020).
- [52] C. Riplinger and F. Neese, An efficient and near linear scaling pair natural orbital based local coupled cluster method, *J. Chem. Phys.* **138**, 34106 (2013).
- [53] J. McClain, Q. Sun, G. K.-L. Chan, and T. C. Berkelbach, Gaussian-Based Coupled-Cluster Theory for the Ground-State and Band Structure of Solids, *J. Chem. Theory Comput.* **13**, 1209 (2017).
- [54] K. Laughon, J. M. Yu, and T. Zhu, Periodic Coupled-Cluster Green’s Function for Photoemission Spectra of Realistic Solids, *J. Phys. Chem. Lett.* **13**, 9122 (2022).
- [55] T. Gruber, K. Liao, T. Tsatsoulis, F. Hummel, and A. Grüneis, Applying the coupled-cluster ansatz to solids and surfaces in the thermodynamic limit, *Phys. Rev. X* **8**, 021043 (2018).

- [56] T. N. Mihm, T. Schäfer, S. K. Ramadugu, L. Weiler, A. Grüneis, and J. J. Shepherd, A shortcut to the thermodynamic limit for quantum many-body calculations of metals, *Nat. Comput. Sci.* **1**, 801 (2021).
- [57] X. Xing and L. Lin, Inverse Volume Scaling of Finite-Size Error in Periodic Coupled Cluster Theory, *Phys. Rev. X* **14**, 011059 (2024).
- [58] S. Sharma, A. A. Holmes, G. Jeanmairet, A. Alavi, and C. J. Umrigar, Semistochastic Heat-Bath Configuration Interaction Method: Selected Configuration Interaction with Semistochastic Perturbation Theory, *J. Chem. Theory Comput.* **13**, 1595 (2017).
- [59] H.-Z. Ye and T. C. Berkelbach, Correlation-Consistent Gaussian Basis Sets for Solids Made Simple, *J. Chem. Theory Comput.* **18**, 1595 (2022).
- [60] C. Hartwigsen, S. Goedecker, and J. Hutter, Relativistic Separable Dual-Space Gaussian Pseudopotentials from H to Rn, *Phys. Rev. B* **58**, 3641 (1998).
- [61] J. VandeVondele, M. Krack, F. Mohamed, M. Parrinello, T. Chassaing, and J. Hutter, Quickstep: Fast and Accurate Density Functional Calculations Using a Mixed Gaussian and Plane Waves Approach, *Comput. Phys. Commun.* **167**, 103 (2005).
- [62] E. A. Vo, X. Wang, and T. C. Berkelbach, Performance of Periodic EOM-CCSD for Bandgaps of Inorganic Semiconductors and Insulators, *J. Chem. Phys.* **160**, 044106 (2024).
- [63] Q. Sun, T. C. Berkelbach, N. S. Blunt, G. H. Booth, S. Guo, Z. Li, J. Liu, J. D. McClain, E. R. Sayfutyarova, S. Sharma, S. Wouters, and G. K. L. Chan, PySCF: the Python-based simulations of chemistry framework, *Wiley Interdiscip. Rev. Comput. Mol. Sci.* **8**, e1340 (2018).
- [64] Q. Sun, X. Zhang, S. Banerjee, P. Bao, M. Barbry, N. S. Blunt, N. A. Bogdanov, G. H. Booth, J. Chen, Z. H. Cui, J. J. Eriksen, Y. Gao, S. Guo, J. Hermann, M. R. Hermes, K. Koh, P. Koval, S. Lehtola, Z. Li, J. Liu, N. Mardirossian, J. D. McClain, M. Motta, B. Mussard, H. Q. Pham, A. Pulkin, W. Purwanto, P. J. Robinson, E. Ronca, E. R. Sayfutyarova, M. Scheurer, H. F. Schurkus, J. E. Smith, C. Sun, S. N. Sun, S. Upadhyay, L. K. Wagner, X. Wang, A. White, J. D. Whitfield, M. J. Williamson, S. Wouters, J. Yang, J. M. Yu, T. Zhu, T. C. Berkelbach, S. Sharma, A. Y. Sokolov, and G. K. L. Chan, Recent developments in the PySCF program package, *J. Chem. Phys.* **153**, 024109 (2020).
- [65] X. Ren, F. Merz, H. Jiang, Y. Yao, M. Rampp, H. Lederer, V. Blum, and M. Scheffler, All-Electron Periodic G_0W_0 Implementation with Numerical Atomic Orbital Basis Functions: Algorithm and Benchmarks, *Phys. Rev. Mater.* **5**, 013807 (2021).
- [66] G. Kang, Y. Kang, and S. Han, Influence of Wave-Function Updates in GW Calculations on Titanates, *Phys. Rev. B* **91**, 155141 (2015).
- [67] C. Bhandari, M. van Schilfhaarde, T. Kotani, and W. R. L. Lambrecht, All-Electron Quasiparticle Self-Consistent GW Band Structures for SrTiO_3 Including Lattice Polarization Corrections in Different Phases, *Phys. Rev. Mater.* **2**, 013807 (2018).
- [68] F. Weigend and R. Ahlrichs, Balanced basis sets of split valence, triple zeta valence and quadruple zeta valence quality for H to Rn: Design and assessment of accuracy, *Phys. Chem. Chem. Phys.* **7**, 3297 (2005).

- [69] K. van Benthem, C. Elsässer, and R. H. French, Bulk Electronic Structure of SrTiO₃: Experiment and Theory, *J. Appl. Phys.* **90**, 6156 (2001).
- [70] I.-W. Lyo and E. W. Plummer, Quasiparticle Band Structure of Na and Simple Metals, *Phys. Rev. Lett.* **60**, 1558 (1988).
- [71] D. V. Potorochin, R. Kurlito, O. J. Clark, E. D. L. Rienks, J. Sánchez-Barriga, F. Roth, V. Voroshnin, A. Fedorov, W. Eberhardt, B. Büchner, and J. Fink, Lifetime of Quasiparticles in the Nearly Free Electron Metal Sodium, *Phys. Rev. B* **106**, 125138 (2022).
- [72] J. McClain, J. Lischner, T. Watson, D. A. Matthews, E. Ronca, S. G. Louie, T. C. Berkelbach, and G. K.-L. Chan, Spectral Functions of the Uniform Electron Gas via Coupled-Cluster Theory and Comparison to the *GW* and Related Approximations, *Phys. Rev. B* **93**, 235139 (2016).
- [73] S. Mandal, K. Haule, K. M. Rabe, and D. Vanderbilt, Electronic Correlation in Nearly Free Electron Metals with Beyond-DFT Methods, *npj Comput. Mater.* **8**, 1 (2022).
- [74] J. S. Zhou, M. Gatti, J. J. Kas, J. J. Rehr, and L. Reining, Cumulant Green's Function Calculations of Plasmon Satellites in Bulk Sodium: Influence of Screening and the Crystal Environment, *Phys. Rev. B* **97**, 035137 (2018).
- [75] L. Craco and S. Leoni, LDA+DMFT Approach to Electronic Structure of Sodium Metal, *Phys. Rev. B* **100**, 115156 (2019).
- [76] J. Lischner, T. Bazhiron, A. H. MacDonald, M. L. Cohen, and S. G. Louie, Effect of spin fluctuations on quasiparticle excitations: First-principles theory and application to sodium and lithium, *Phys. Rev. B* **89**, 81108 (2014).
- [77] S. Wouters, C. A. Jiménez-Hoyos, Q. Sun, and G. K.-L. Chan, A Practical Guide to Density Matrix Embedding Theory in Quantum Chemistry, *J. Chem. Theory Comput.* **12**, 2706 (2016).
- [78] F. Aquilante, T. K. Todorova, L. Gagliardi, T. B. Pedersen, and B. O. Roos, Systematic Truncation of the Virtual Space in Multiconfigurational Perturbation Theory, *J. Chem. Phys.* **131**, 034113 (2009).
- [79] H. J. A. Jensen, P. Jorgensen, H. Ågren, and J. Olsen, Second-order Moller-Plesset Perturbation Theory as a Configuration and Orbital Generator in Multiconfiguration Self-consistent Field Calculations, *J. Chem. Phys.* **88**, 3834 (1988).
- [80] D. Mester, P. R. Nagy, and M. Kállay, Reduced-Cost Linear-Response CC2 Method Based on Natural Orbitals and Natural Auxiliary Functions, *J. Chem. Phys.* **146**, 194102 (2017).
- [81] B. T. G. Lau, B. Busemeyer, and T. C. Berkelbach, Optical Properties of Defects in Solids via Quantum Embedding with Good Active Space Orbitals, *J. Phys. Chem. C* **128**, 2959 (2024).